Supplement of Atmos. Chem. Phys., 25, 11087–11107, 2025
https://doi.org/10.5194/acp-25-11087-2025-supplement

Atmospheric Chemistry and Physics
Open Access

Supplement of

Atmospheric chemistry in East Asia determines the iron solubility of aerosol particles supplied to the North Pacific Ocean

Kohei Sakata et al.

Correspondence to: Kohei Sakata (kohei.sakata.33@mail.dendai.ac.jp)

S1. Supplemental Note

S1.1 Source apportionment of T-Fe and d-Fe sourcesb by a diagram of $EF_{T\text{-}Fe}$ and [d-Fe]/[d-Al]

In the first group, T-Fe is primarily associated with mineral dust ($EF_{T\text{-}Fe} < 2.0$). Under conditions of proton-promoted dissolution, the [d-Fe]/[d-Al] ratios of aluminosilicate minerals (*e.g.*, biotite, illite, and chlorite) were ranged from 0.14 to1.03 (Kodama and Schnitzer, 1973; Lowson et al., 2005; Bibi et al., 2011; Bray et al., 2015). Furthermore, the [d-Fe]/[d-Al] ratio of Asian dust was 0.24 ± 0.20 (Duvall et al., 2008). From these reported values, the range of [d-Fe]/[d-Al] ratio of proton-promoted dissolution of mineral dust was defined from 0.10 to 1.00 (brown area in Fig. 2). The T-Fe in the second group is also derived from mineral dust, but the d-Fe in this group is mainly dissolved by ligand-promoted dissolution. The [d-Fe]/[d-Al] ratio in the group exceeds 1.0 owing to the preferential complexation of iron by organic ligands over Al (green area in Fig. 2, Kodama and Schnitzer, 1973; Bray et al., 2015). Third group represents a binary mixing of mineral dust and insoluble anthro-Fe, which is characterized by $EF_{T\text{-}Fe} > 2.0$ and a [d-Fe]/[d-Al] ratio <1.00 (white area in Fig. 2). Here, anthro-Fe refers to anthropogenic Fe-rich particles that can increase $EF_{T\text{-}Fe}$, including Fe-oxide nanoparticles, which emits from not only high-temperature combustion processes (*e.g.*, steel industry, coal combustion; Ito et al., 2021) but also non-combustion sources such as debris from automobile brake pads (Li et al., 2022; Fu et al., 2023). The anthro-Fe present in this group exhibits low solubility and thus makes a negligible contribution to the increase in the [d-Fe]/[d-Al] ratio observed in the aerosols. Therefore, it is inferred that the d-Fe primarily reflects the values characteristic of mineral particles with which the insoluble anthro-Fe is associated. Unlike third group, the [d-Fe]/[d-Al] ratio in the fourth group is greater than 1.0 because of the high Fe_{sol}% of anthro-Fe. As a result, the fourth group is characterized by aerosols where both T-Fe and d-Fe are influenced by anthro-Fe. (grey area in Fig. 2). Although earlier studies suggest that oxalate leaching leads to a higher [d-Fe]/[d-Al] ratio for anthro-Fe compared to acid leaching, a distinct threshold to differentiate these processes is currently lacking. As a result, unlike with mineral dust, it is difficult to determine anthro-Fe was dissolved via proton-promoted or ligand-promoted dissolution based on the diagram. Finally, final group is aluminosilicate glasses emitted from high-temperature combustions, including coal combustions. It is known that aluminosilicate glasses were emitted from high-temperature combustions, which can be characterized low $EF_{T\text{-}Fe}$ (< 2.0) and [d-Fe]/[d-Al] ratio (<0.10), which are totally different those for anthropogenic Fe-rich particles. Thus, one of the key advantages of this method lies in its capacity to discriminate between anthropogenic Fe-rich particles and aluminosilicate glasses produced by high-temperature combustion processes.

S1.2 Positive matrix factorization

The input file for PMF analysis was concentrations of target species and their uncertainties. Uncertainties of each element were evaluated by the following equations:

$$Uncertainty = \frac{5}{6} \times MDL \quad \text{(Eq. S1)}$$

$$Uncertainty = \sqrt{(Error\ fraction\ \times concentraion)^2 + (0.5 \times MDL)^2} \quad \text{(Eq. S2)}$$

where MDL is the method detection limit, defined as three times the standard deviation of the filter blank concentration. Equations S1 and S2 were used when target species concentrations were lower and higher than MDL, respectively. The PMF analysis allows for three categories: “Strong”, “Weak”, and “Bad”. These categories were typically chosen based on the signal-to-noise (S/N) ratio. The “Weak” category is selected when the S/N is between 0.5 and 1.0, and the “Bad” category is used if the S/N ratio is lower than 0.5. Species classified as "Weak" had their associated uncertainties tripled, and species classified as "Bad" were excluded from further analysis. Initially, PMF analysis was performed with all elemental categories set to “Strong” because the S/N for all species was higher than 7.0. Consequently, the coefficient of determination (r^2) between the observed and modeled concentrations of the input species was greater than 0.60, with the exception of Cr in the EAout period (Tables S4 and S5). The PMF analysis for the EAout period was then rerun with the Cr category set to "Weak," but the results did not change significantly. Therefore, this study employed the PMF results with all species categories set to "Strong," based on the conventional use of the S/N ratio for category determination.

S1.3 Macroscopic and microscopic XANES

Macroscopic X-ray absorption near-edge structure (XANES) spectra were recorded at beamlines of BL-9A and BL-12C in Photon Factory. The synchrotron radiation generated by the bending magnet was monochromatized by a double-crystal monochromator of Si(111). The XANES experiment were performed in ambient air at room temperature. Approximately one-tenth of collected aerosol particles on PTFE filters were transferred to a double-face carbon tape. The aerosol samples were oriented at 45° to the incident X-ray beam. The incident X-ray energy was calibrated with the peak top of the pre-edge peak of the nonderivative Fe K-edge XANES spectrum for hematite aligned to 7112 eV. All XANES spectra of aerosol samples were recorded in fluorescence yield mode. Fluorescence X-ray from the aerosol sample was detected with a seven-element silicon drift detector equipped with a Soller slit to reduce elastic X-ray around the beam pass. The front face of the Soller slit was covered with a 0.2 mm-thick PTFE filter to remove fluorescence X-rays of coexisted elements (*e.g.*, Ca and Mn) and argon in the ambient air. Linear combination fitting of the XANES spectra of aerosol samples using reference materials was performed with REX2000 software. The fitting was performed over the energy range of 7100–7200 eV. The goodness of fit was evaluated by the following equation:

$$\Sigma R = \frac{\Sigma[I_{obs}(E) - I_{cal}(E)]^2}{\Sigma[I_{obs}(E)]^2} \qquad \text{(Eq. S3)}$$

where $I_{obs}(E)$ and $I_{cal}(E)$ are X-ray absorption of the normalized X-ray absorptions of the samples and the calculated values at each energy.

The μ-XRF-XANES analyses were performed at BL-15A1 in PF. Aerosol samples with sizes of 0.39–0.69 μm and 2.1–4.2 μm, collected in September 2019, were used for the μ-XRF-XANES analyses. The beam size at the sampling position (20×20 μm^2) is larger than the aerodynamic diameter of the target samples. Although these experiments were not single-particle analyses, spot analysis combined with XRF mapping allows for the identification of chemical species of target elements from different emission sources (*e.g.*, mineral and non-mineral materials). Aerosol particles on the carbon tape were mounted on an acrylic sample holder and oriented at 45° to the direction of the incident X-ray beam. XRF maps of the 3d transition metals (Mn, Fe, Ni, Cu, and Zn) and light elements (Ti, Ca, K, Cl, and S) were acquired using a raster scan of the sample stage irradiated with 14 and 5.1 keV incident X-rays, respectively. Measurement spots for Fe species were selected based on the XRF maps of the target elements normalized by the incident X-ray intensity. Iron K-edge XANES spectra of the regions of interest were recorded in quick-scan mode with a scan time of 180 sec. The same spectral analysis procedure used for macroscopic XANES was applied to the micro-focused XANES data.

S2. Assignment of emission sources to each factor obtained in the PMF

S2.1 Validation of PMF result by comparison of JPN and EAout periods with entire period (JPN+EAout)

The six factors were identified as the source of fine aerosol particles for the entire (JPN+EAout) period: (i) sea spray aerosol and fresh dust, (ii) aged mineral and road dust, (iii) steel industry, (iv) heavy oil combustion, (v) non-ferrous industry, and (iv) secondary aerosol. For the JPN period, the same factor was identified as the dominant source of fine aerosol particles. In contrast, heavy oil combustion was not the source of fine aerosol particles. This is a reasonable result because the PMF analysis of the JPN+EAout period showed a small contribution of the non-ferrous industry in the EAout period. The time trend of the normalized factor contributions combined with the JPN and EAout period well correlated with those obtained by PMF analysis for the entire period. Therefore, the PMFs conducted in this study are considered to have reasonable results.

S2.2 Sea spray aerosol and fresh dust

The factor was characterized by the large contributions of Na and Mg as typical tracer elements of sea spray aerosol (SSA, Fig. S8a and S9a). Since aerosol sampling was performed in the coastal regions, the presence of the factor of SSA is a reasonable result. In addition, Al, Ti, and Fe were also assigned as the dominant components of the factor (Fig. S8a and S9a). The PMF estimated $EF_{T\text{-}Fe}$ in this factor is almost 1.0 (JPN: 1.6, EAout: 0.86), indicating that mineral dust also contributed as the source of the factor. The normalized contribution of this factor increases with increasing aerosol diameter, consistent with the amount of physically resuspended particles being dominated by coarse aerosol particles. Furthermore, there was no clear seasonal trend in the normalized factor contribution, suggesting that the factor was influenced by local emission sources near the sampling site. The contribution of the local source to this factor is supported by the fact that the PMF-estimated [nss-SO_4^{2-}]/[T-Fe] for both periods were 0 (Table S3 and S4), indicating that aerosol particles in this factor were not aged in the atmosphere (= these particles were collected immediately after their release into the atmosphere). In this factor, small contributions (<20%) to total concentration in fine aerosol particles) of Cu, Zn, Cd, and Pb were found in the factor. PMF-estimated EF of these elements was higher than 10, indicating that these elements were derived from anthropogenic sources. These elements were derived from anthropogenic emissions of non-exhaust vehicle particles in road dust rather than high-temperature combustion because road dust was also physically resuspended aerosol particles, including SSA and mineral dust. It is known that Cu and Zn in road dust were derived from debris of brake rings and tire wear in road dust, respectively (Birmili et al., 2006; Apeagyei et al., 2011; Shupert et al., 2013). The paint of road signs was the source of Pb in road dust (Adachi and Tainosho, 2004; Sakata et al., 2014; Halle et al., 2021).

S2.3 Aged mineral and road dust

The factors characterized by the high contribution of Al, Ti, and Fe as typical tracer elements of mineral dust, whereas the contribution of Na and Mg was not confirmed. The normalized factor These results indicated that the factor was influenced by mineral dust. The normalized contribution factor of this factor is the highest and lowest in the fractions of 0.69–1.3 μm and <0.39 μm, respectively. The normalized factor contribution was higher from February to April when Asian dust was transported from East Asia. Therefore, the factor was influenced by mineral dust that underwent long-range transportation. Mineral dust in the factor was aged in the atmosphere because the [nss-SO_4^{2-}]/[T-Fe] for both periods were not 0. Indeed, the Fe_{sol}% in the factor (JPN: 60.6%, EAout: 19.3%) was higher than Fesol% in SSA and fresh dust factor (JPN: 17.1%, EAout: 0%). The $EF_{T\text{-}Fe}$ in the factor for the JPN and EAout periods were 2.14 and 1.30, respectively, indicating that anthro-Fe contributed as the source of T-Fe. Small contributions of Cu, Zn, Cd, and Pb were found in the factor, of which EFs were higher than 10. These elements are thought to be derived from road dust for the same reasons as the SSA and fresh dust factors. Anthro-Fe is present in addition to the factor of SSA and fresh dust. Especially for the JPN period, the $EF_{T\text{-}Fe}$ of this factor was 2.1, indicating that anthro-Fe was one of the dominant sources of Fe. As proof, approximately 20% of anthro-Fe in fine aerosol particles collected for the JPN period was derived from this factor. The contribution of road dust to anthro-Fe in fine aerosol particles was consistent with the source apportionment of anthro-Fe in Japanese $PM_{2.5}$ by a semi-bottom-up model (Kajino et al., 2020).

S2.4 Steel industry

The factor was characterized by high contributions of tracer elements for anthropogenic emissions (e.g., Mn, Cr, Ni, Cu, Zn, Cd, and Pb). These elements, especially Mn and Cr, were often used as the tracer elements of the steel industry (An et al., 2015; Liu et al., 2018; Zheng et al., 2020; R. Li et al., 2021). Furthermore, the highest contribution of anthro-Fe for the JPN and EAout period was found in the factor. Model calculations of emission sources of metal elements using a semi-bottom-up model showed that anthro-Fe in Japanese $PM_{2.5}$ is mainly derived from the steel industry and non-exhaust vehicle emissions (Kajino et al., 2020). In the case of the EAout period, approximately 90% of anthropogenic magnetic particles in $PM_{2.5}$ in China (mainly composed of magnetite) were emitted from iron and steel making (S. Li et al., 2021). Furthermore, about 60% of anthro-Fe has been emitted from the steel industry in China (Chen et al., 2021). Therefore, the factor was attributed to the emission of the steel industry. One concern is that the normalized contribution of the factor was often highest in the 0.69–1.3 μm fraction, even though the normalized contributions of other factors associated with anthropogenic emissions were the highest in <0.39 μm or 0.39–0.69 μm fractions (Figure S7d–S7e). A recent study examined the size-distributions of mass concentration of Fe emitted from various processes in the steel industry (e.g., sintering, puddling, and steel-making). As a result, the mass concentration of Fe yields a bimodal distribution, of which concentration peaks were in coarse and fine aerosol particles. Furthermore, the concentration peak of fine aerosol particles was found in the 0.65-1.1 μm fraction (Jia et al., 2018), consistent with the largest fraction of this factor. Therefore, we concluded that this factor was influenced by metal elements emitted from the steel industry.

S2.5 Secondary aerosol

This factor was characterized by a large contribution of SO_4^{2-}, whereas contributions of the tracer elements for SSA, mineral dust, and anthropogenic aerosol were not high (<20%). It is known that sulfates in fine aerosol particles were mainly formed secondarily by the aqueous-phase chemistry in cloud water and aerosol liquid water on the particle surface (e.g., oxidation of SO_2, Li et al., 2020; Liu et al., 2021; Itahashi et al., 2022). As markers of primary sources, K, Zn, Cd, and Pb as the tracers of coal combustion was found in the factor. This is a reasonable result because SO_2 as the precursor of sulfate aerosol is mainly emitted from these anthropogenic emissions (Wang et al., 2014; Kurokawa and Ohara, 2020). The specific feature of this factor was a significant contribution to d-Fe in fine aerosol particles. As discussed in the manuscript, this factor contributed as a dominant source of d-Fe in fine aerosol particles, which is attributed to Fe solubilization by aqueous-phase chemistry and surface reaction. Recently, transition-metal ion-catalyzed oxidation are important to sulfate formation in East Asia (Li et al., 2020; Itahashi et al., 2022) and the pathway contributed to sulfate formation at our sampling site (Itahashi et al., 2022). Iron is an important metal ion in driving TMI-catalyzed oxidation, but its effect depends on Fe_{sol}%. The acidification of cloud and aerosol liquid water by the uptake of SO_2 may have caused a synergistic effect that not only enhanced Fe_{sol}% but also promoted sulfate formation. Therefore, the large contribution of d-Fe in this factor is a reasonable result.

S2.6 Heavy oil combustion

The factor is characterized by the high contribution of V and Ni as typical tracers of heavy oil combustions (Kajino et al., 2020, Nriagu and Pacyna, 1988). The normalized contribution factor was high in the JPN period, with little contribution in the EAout period (Fig S7d). Indeed, the heavy oil factor was not assigned as a major component from the PMF analysis using fine aerosol particles collected for the EAout period (Fig. S9). It is known that Fe_{sol}% in fly ash associated with heavy oil combustion was higher than other anthro-Fe sources due to the presence of Fe sulfates with high water solubility (Schroth et al., 2009; Oakes et al., 2012). However, the factor did not contribute as the d-Fe source in fine aerosol particles for both periods due to low concentration of T-Fe (Table S4 and S5).

S21.7 Other industries

Higher contributions of Cr and Ni than other elements were found in the factor for both periods. In the case of the EAout period, contributions of other elements were not significant, whereas high contributions of V, Cu, Zn, and Pb were found for the JPN period. These elements were usually derived from anthropogenic emissions. In contrast, the contributions of T-Fe and anthro-Fe were not significant for both periods. Therefore, these emissions were associated with industrial emissions other than steel industry and coal combustions associated with the secondary aerosol factor. The possible source of the factor is non-ferrous industry. The difference in elemental profiles between the JPN and EAout eras is probably due to differences in the metal species produced (e.g., Pb, Cu-Ni, and Zn-Cd) and their raw materials (Nriagu and Pacyna, 1988).

Supplemental Figure

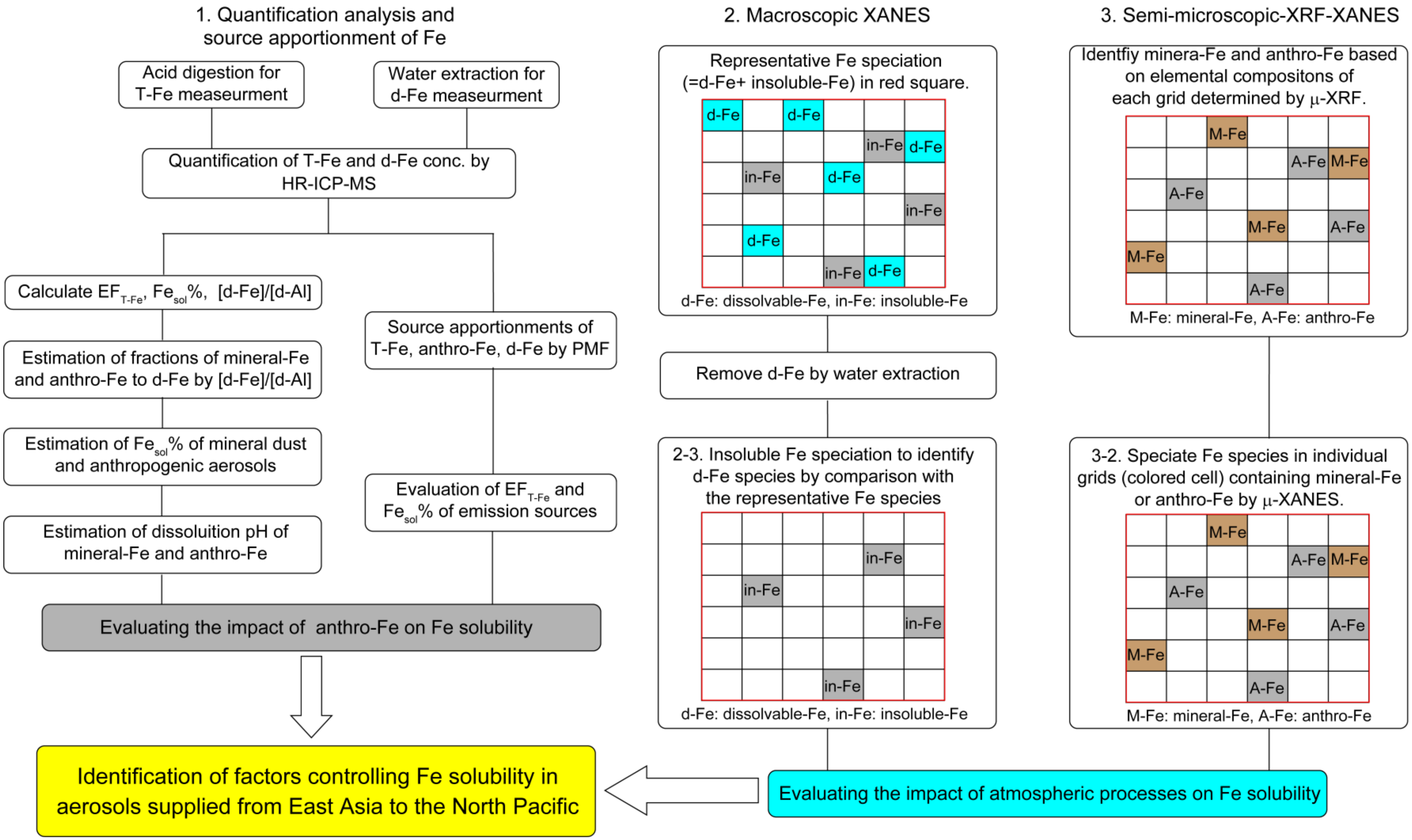

Figure S1 Analytical schemes of source apportionment of Fe based on the quantification analysis and Fe speciation using macroscopic and semi-microscopic XANES spectroscopy.

(a) Japanese air mass (JPN) period

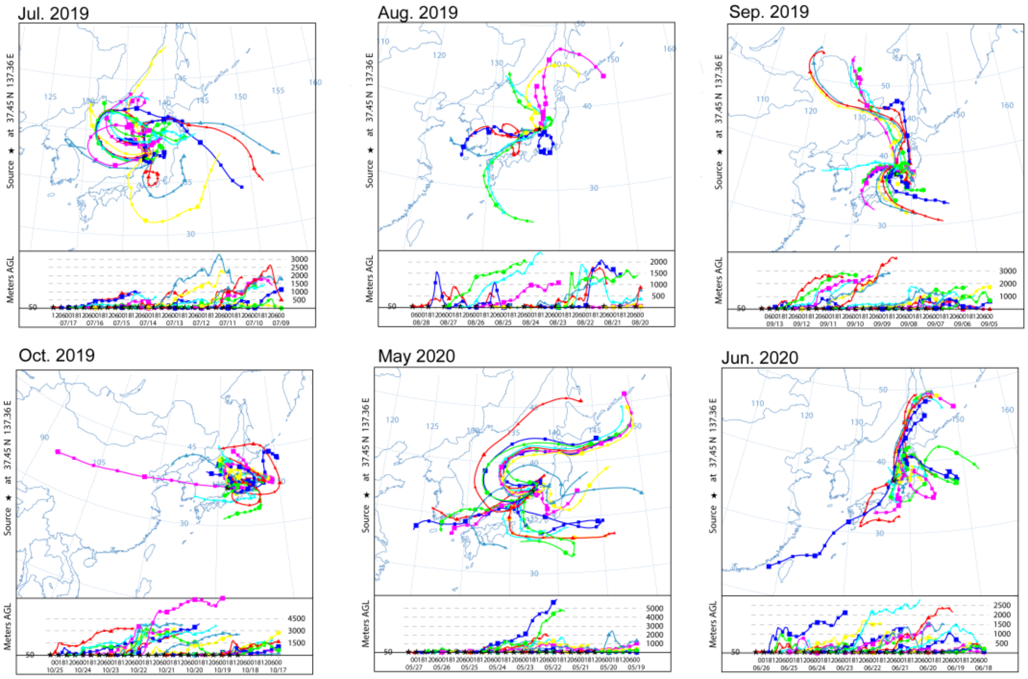
Jul. 2019 Aug. 2019 Sep. 2019 Oct. 2019 May 2020 Jun. 2020

(b) East Asian outflow (EAout) period

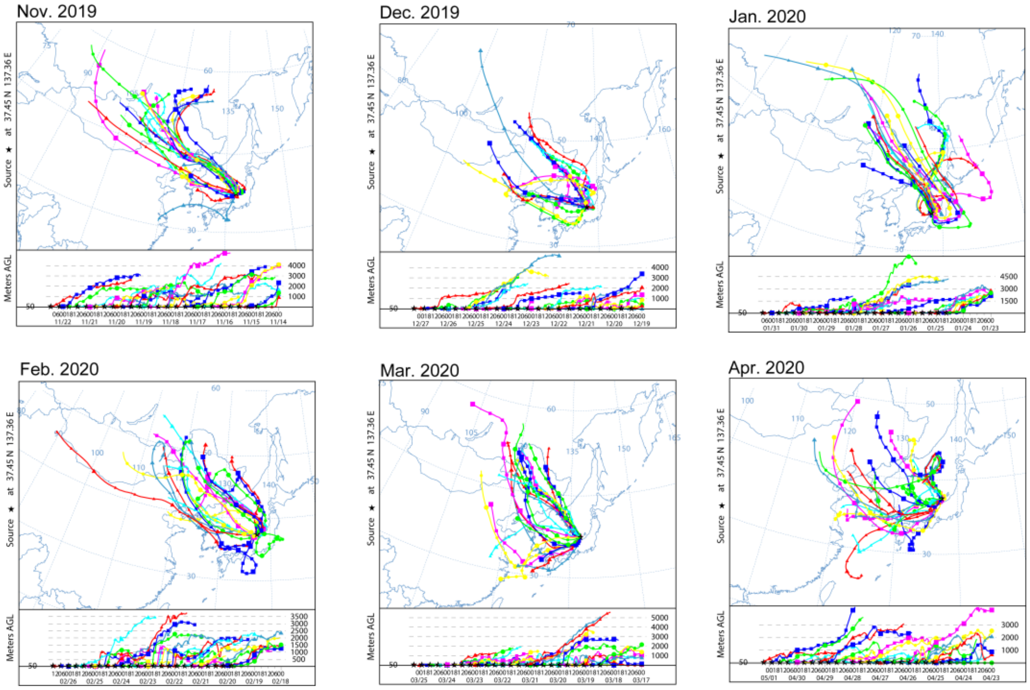
Nov. 2019 Dec. 2019 Jan. 2020 Feb. 2020 Mar. 2020 Apr. 2020

Figure S2. Backward trajectories of at the sampling site during the period of (a) Japanese-air and (b) Asian outflow.

(a) Japanese air mass (JPN) period

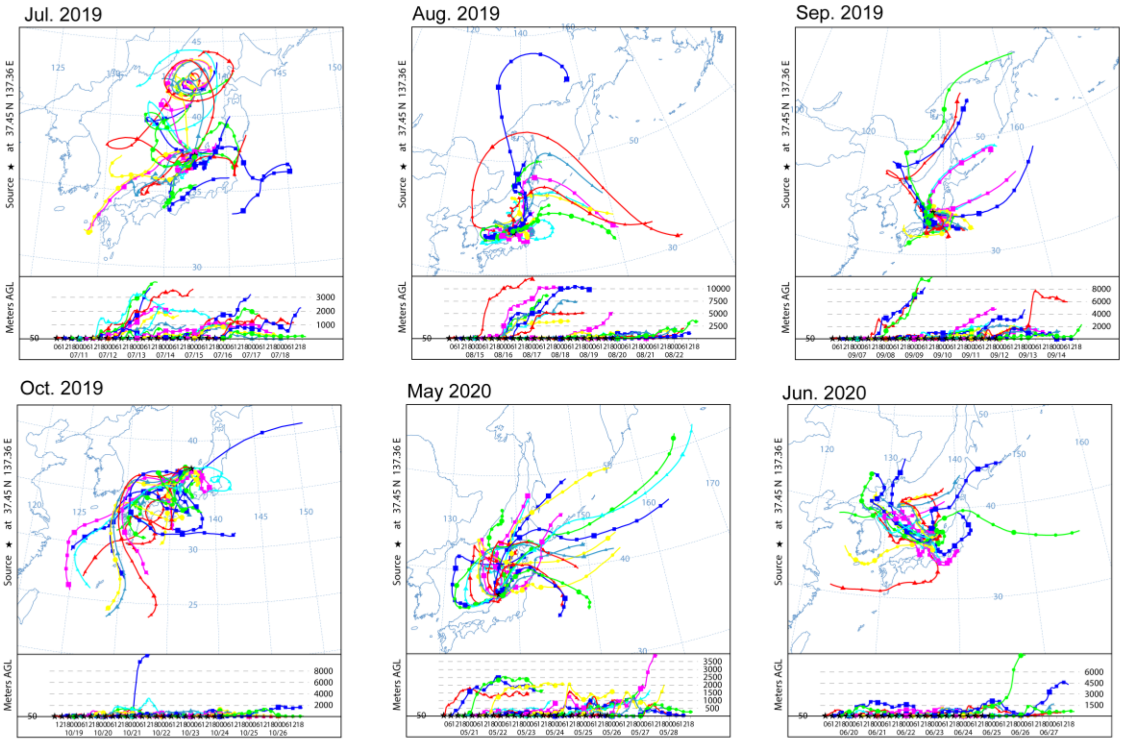

(b) East Asian outflow (EAout) period

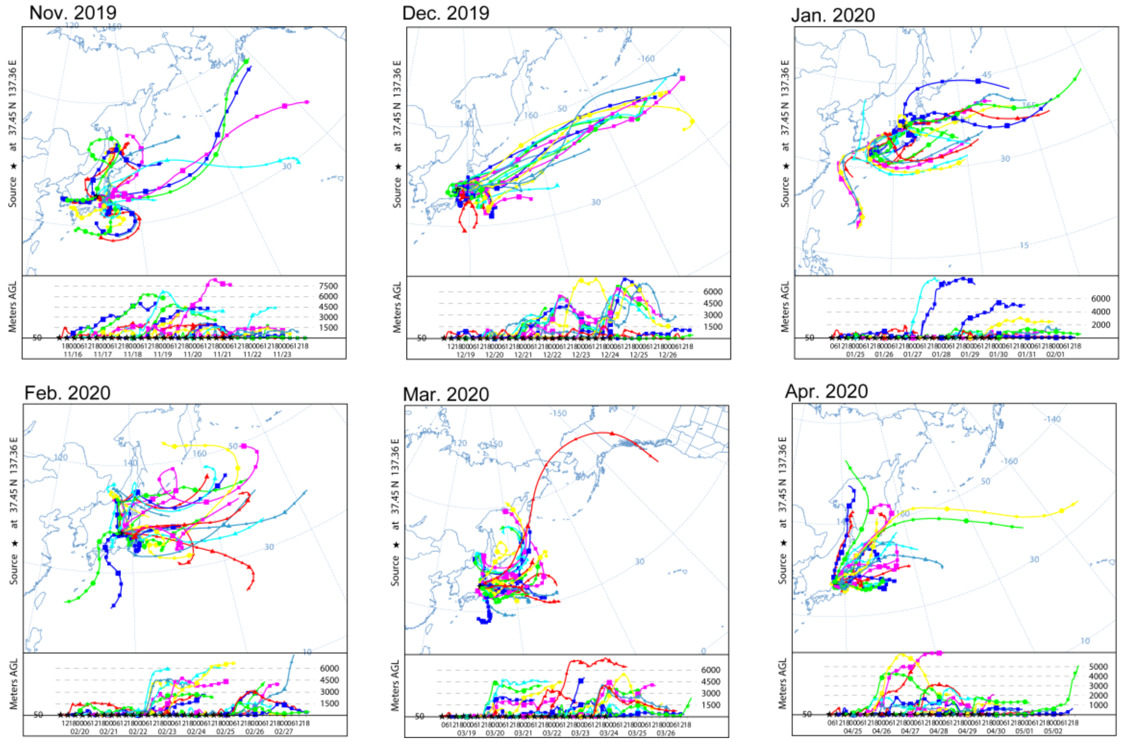

Figure S3. Forward trajectories during the periods of (a) Japanese-air and (b) Asian outflow.

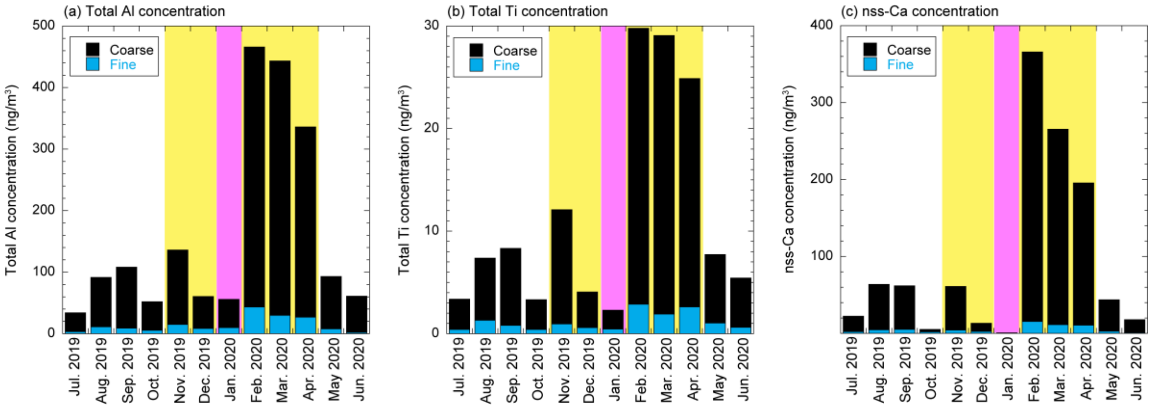

Figure S4. Monthly variations of concentrations of (a) total Al, (b) total Ti, and (c) non-sea-salt (nss) Ca in TSP (black + light blue bars). Black and light blue bars show these concentrations in coarse and fine aerosol particles, respectively. The yellow and pink shaded regions show the EAout and COVID-19 lockdown periods, respectively.

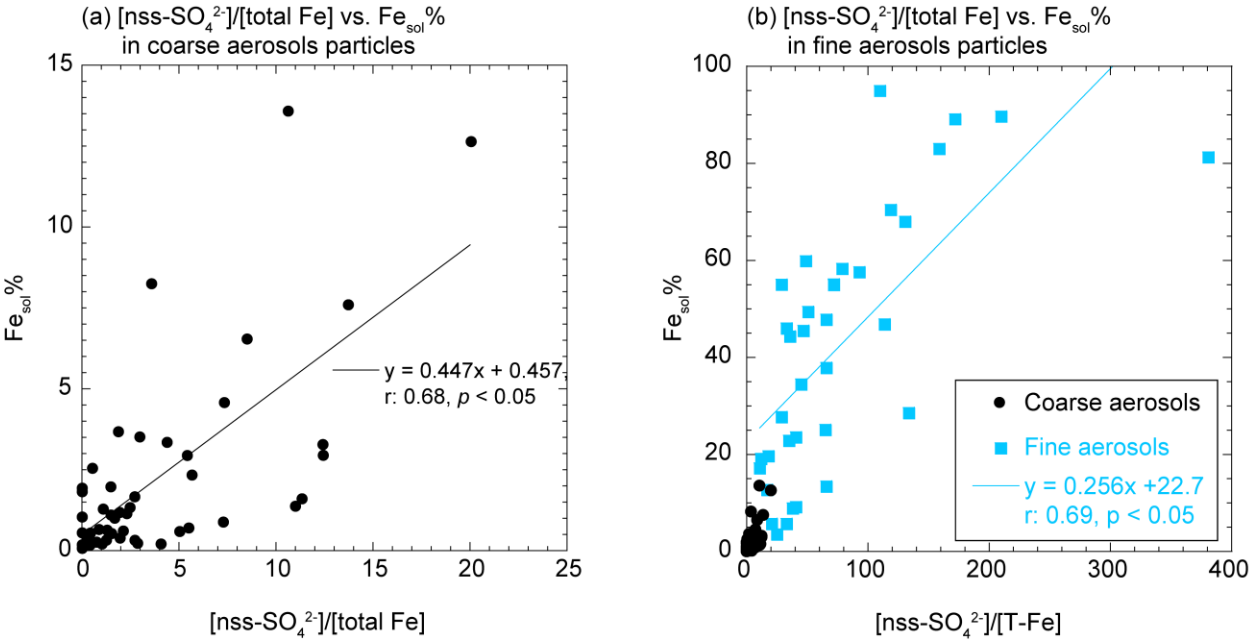

Figure S5. Scatter plots of [nss-SO$_4^{2-}$]/[total Fe] and Fe$_{sol}$% in (a) coarse aerosol particles and (b) fine aerosol particles.

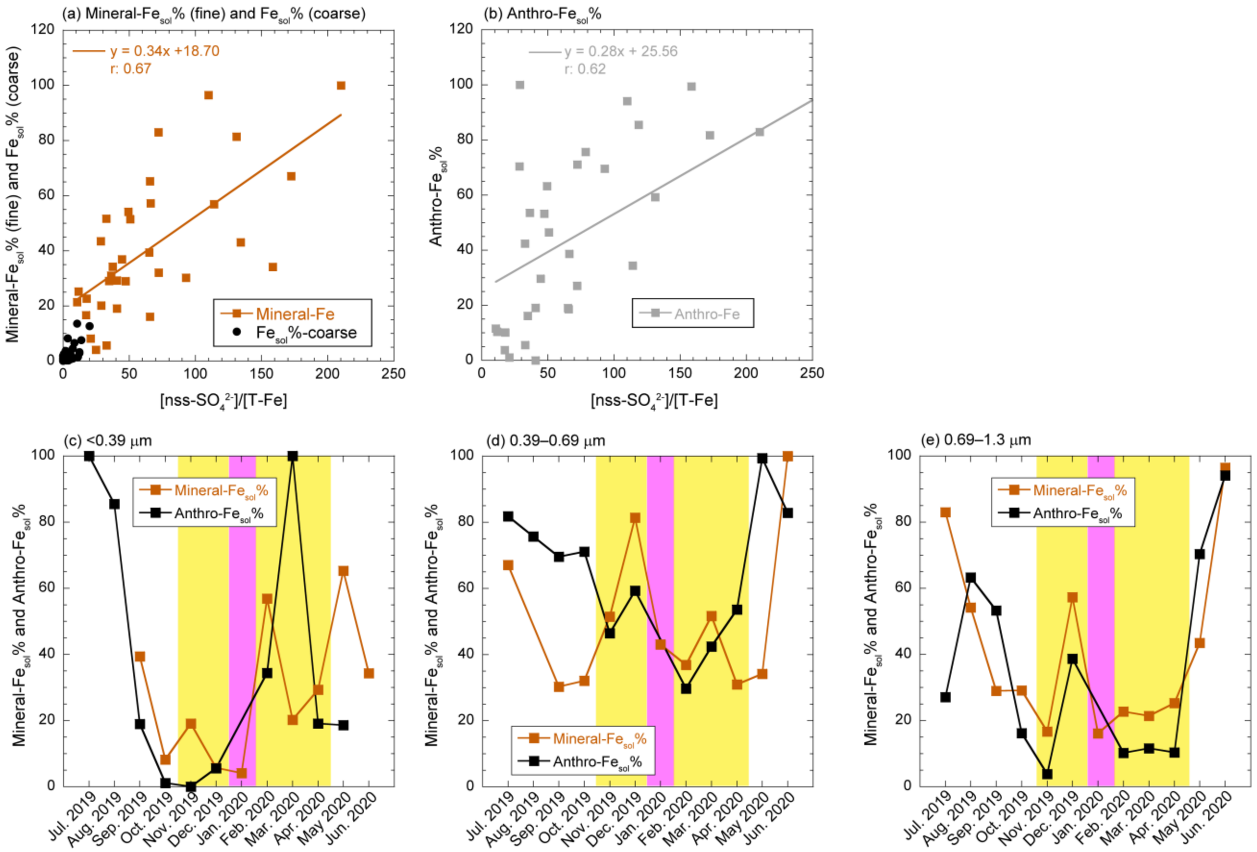

Figure S6. Scatter plots of [nss-SO_4^{2-}]/[T-Fe] with (a) mineral-Fe_{sol}% in fine aerosol particles and Fe_{sol}% in coarse aerosol particles and (b) anthro-Fe_{sol}% in fine aerosol particles. Monthly variations of mineral-Fe_{sol}% and anthro-Fe_{sol}% in (a) <0.39 µm, (b) 0.39–0.69 µm, and (c) 0.69–1.3 µm. Mineral-Fe_{sol}% or anthro-Fe_{sol}% for samples with no contribution of mineral-Fe or anthro-Fe are not plotted. Yellow and pink shaded areas show the EAout and COVID-19 lockdown periods.

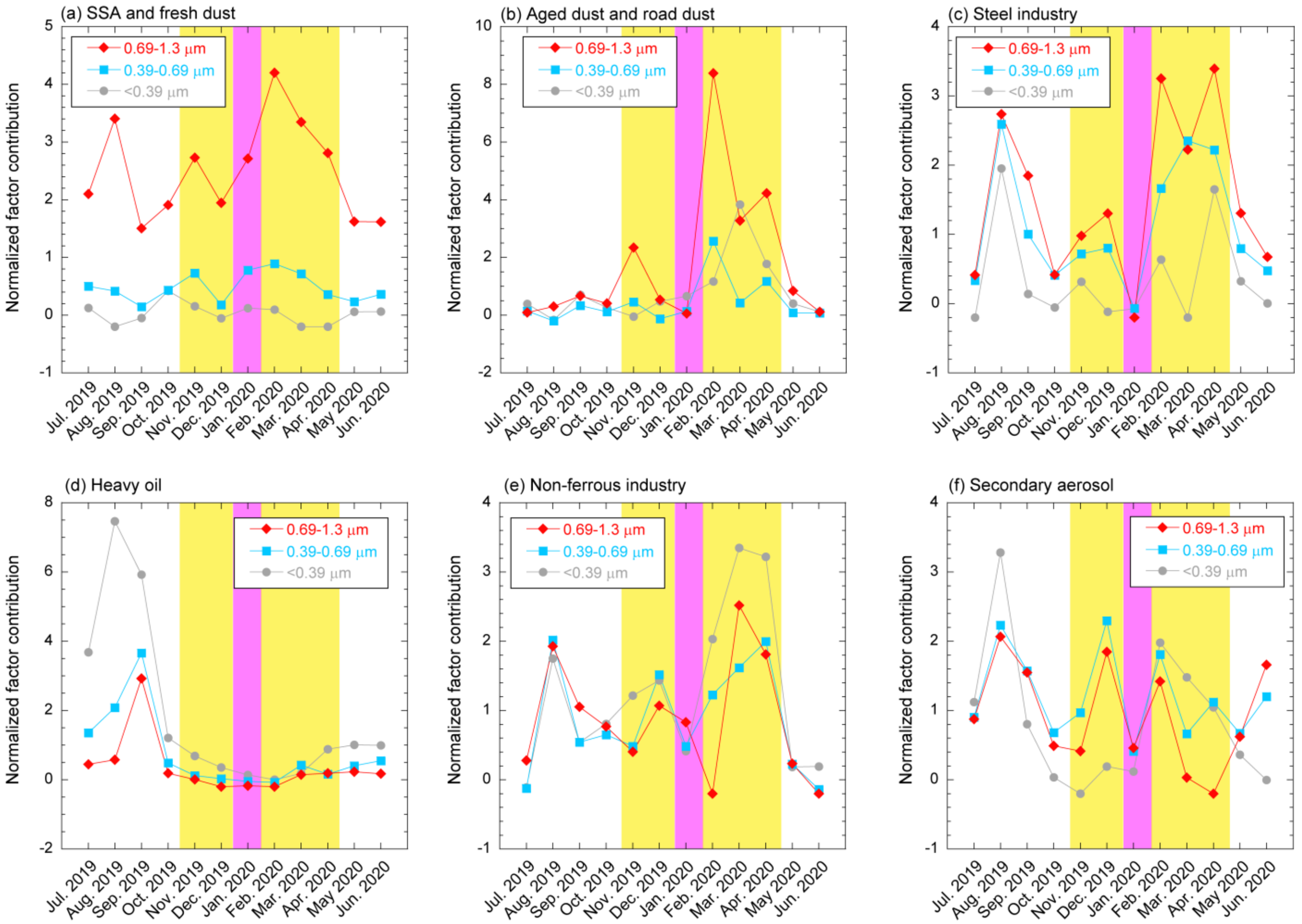

Figure S7. Time trends of the normalized contribution factors of (a) SSA and fresh dust, (b) aged dust and road dust, (c) steel industry, (d) heavy oil, (e) non-ferrous industry, and (f) secondary sulfate. The normalized factor contributions were estimated by PMF analysis for the entire sampling period. Yellow and pink shaded areas show the EAout and COVID-19 lockdown periods.

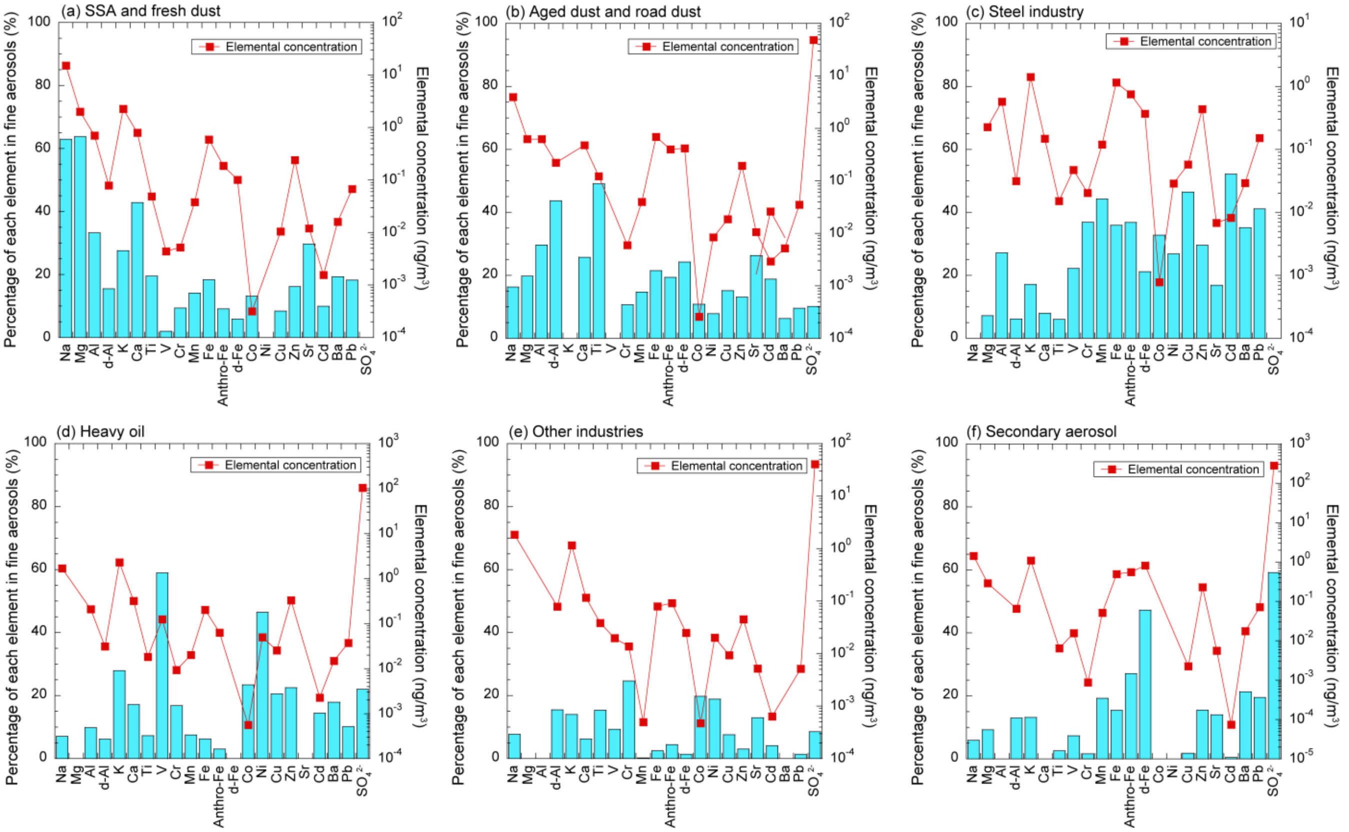

Figure S8. The elemental compositions and their relative contribution to the emission sources of fine aerosol particles in JPN-periods: (a) SSA + fresh dust, (b) aged dust and road dust, (c) steel industry, (d) heavy oil, (e) non-ferrous industry, and (f) secondary aerosol. The bar and line graphs showed the percentages of each element in fine aerosol particles and elemental concentrations, respectively.

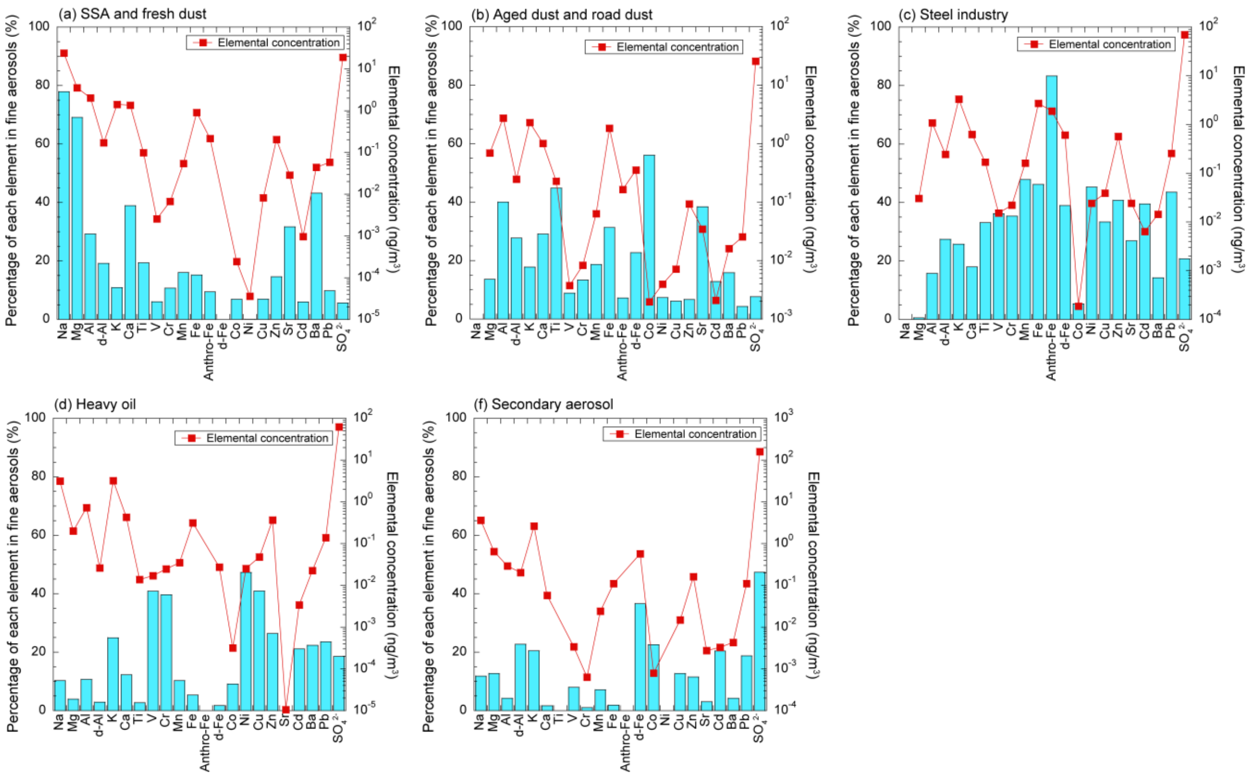

Figure S9. The elemental compositions and their relative contribution to the emission sources of fine aerosol particles in EAout-periods: (a) SSA + fresh dust, (b) aged dust and road dust, (c) steel industry, (d) other industry, and (e) secondary aerosol. The bar and line graphs showed percentages of each element in fine aerosol particles and elemental concentrations, respectively.

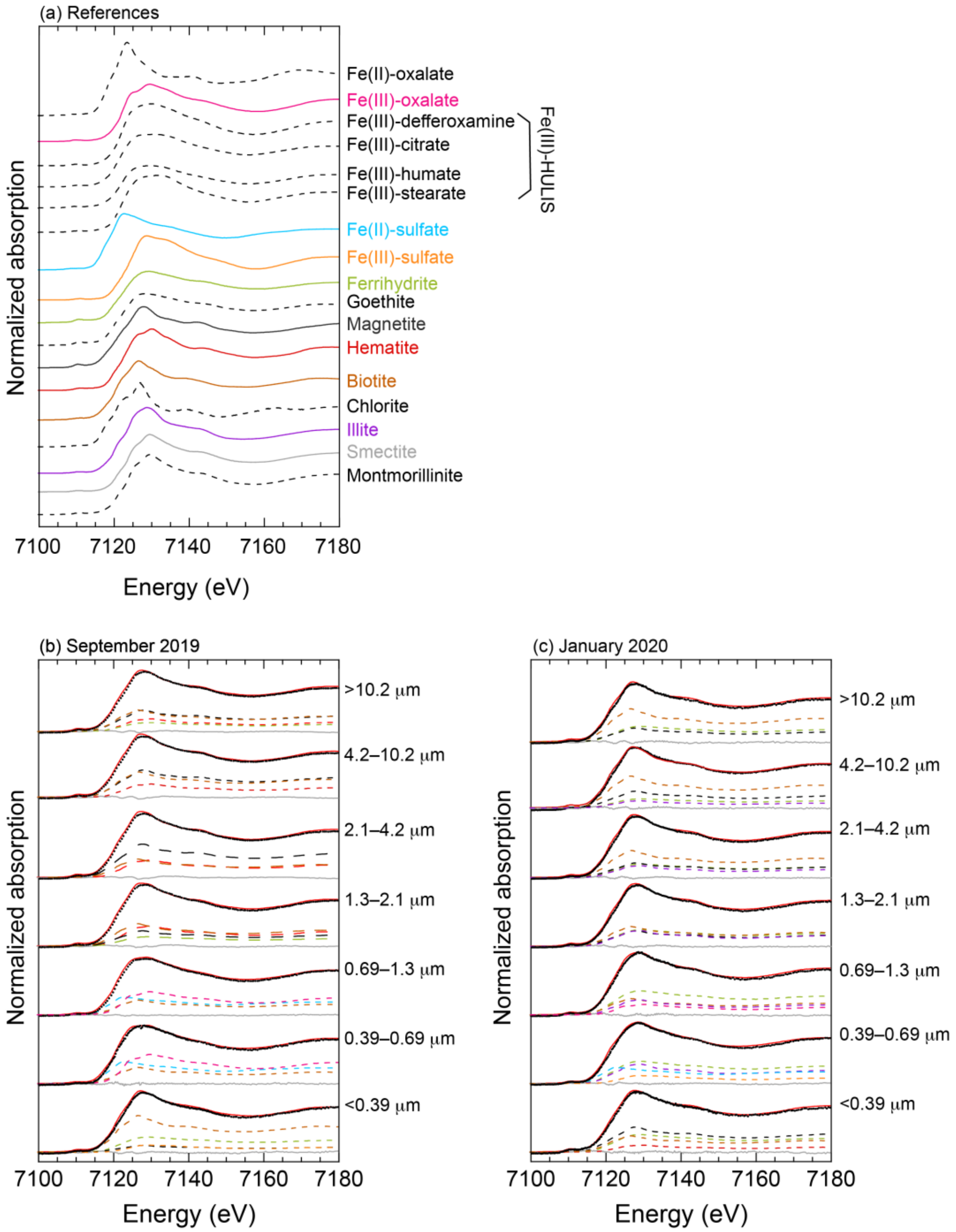

Figure S10. (a) Fe K-edge XANES spectra of the reference materials. The XANES spectra with solid line are the Fe species identified in aerosol particles. The XANES spectra with dashed line are Fe species that are not present in the aerosol particles. Iron K-edge XANES spectra of aerosol particles collected in (b) September 2019 and (c) January 2020. Black dots and solid red lines indicate XANES and fitting spectra of aerosol and aerosol samples, respectively. The colored dashed line shows the XANES spectra of the reference materials, and the colors correspond to panel (a). Solid gray line shows the residual spectrum of the fitting.

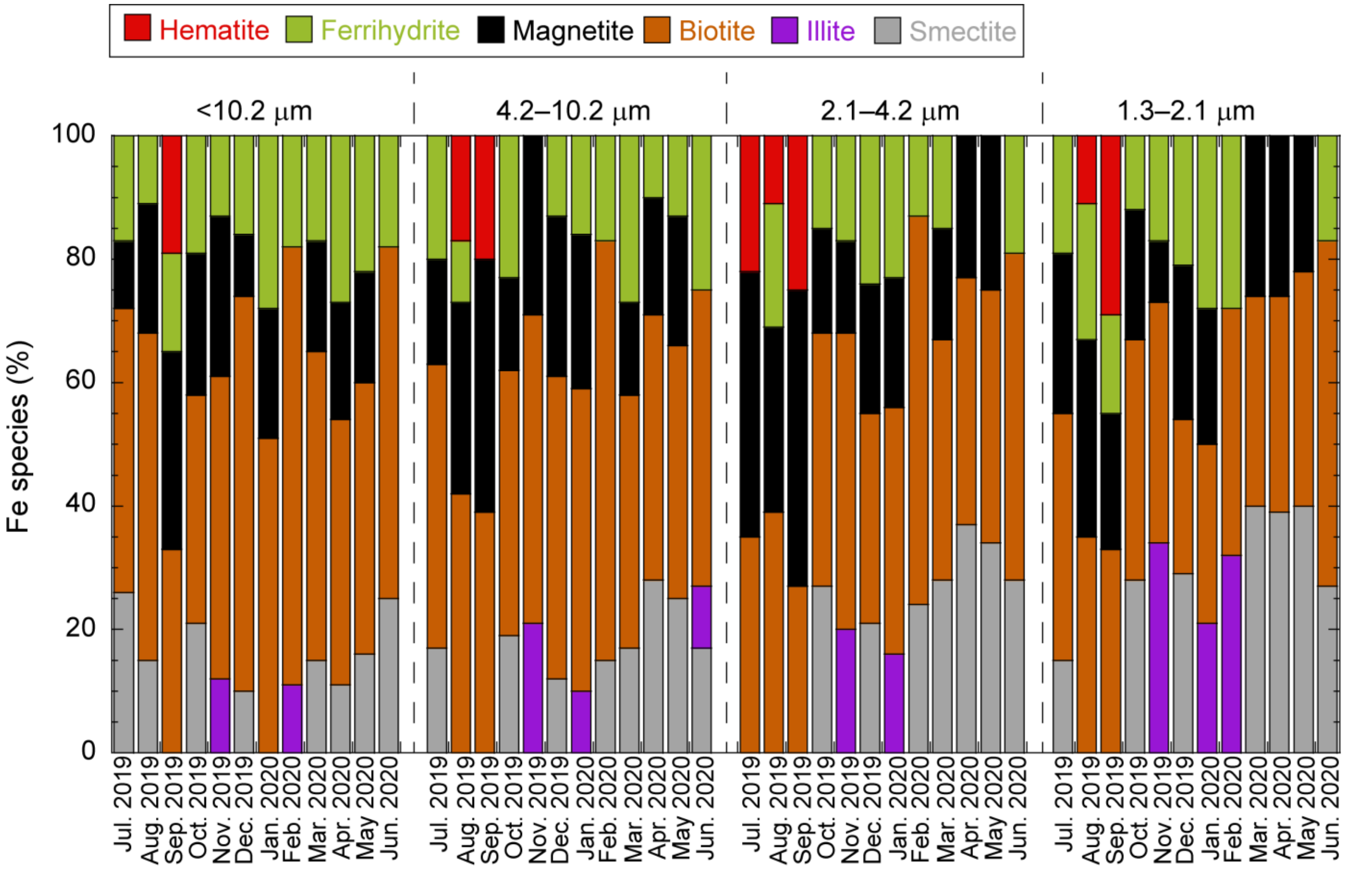

Figure S11. Representative Fe species in coarse aerosol particles determined by macroscopic XANES spectroscopy.

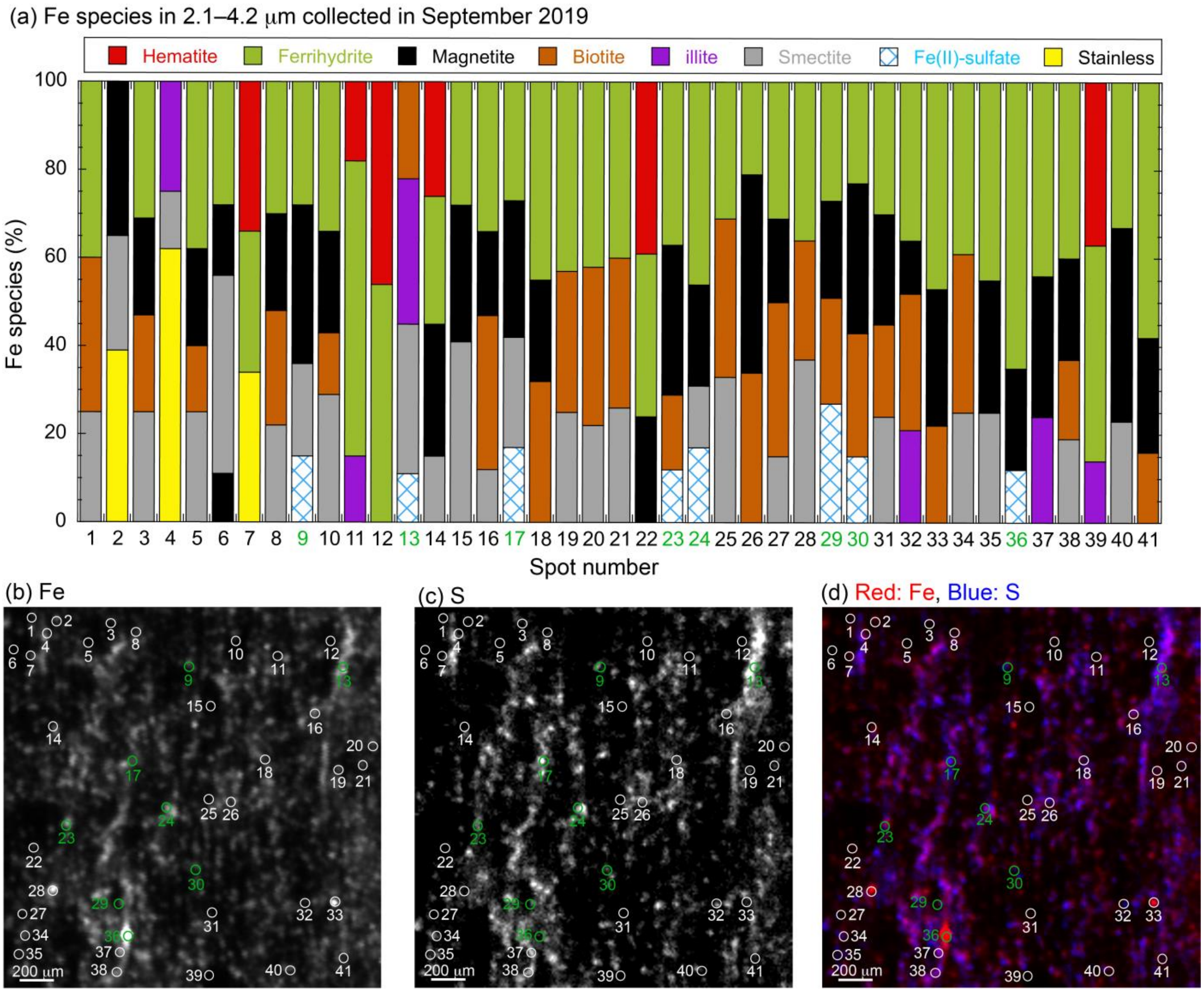

Figure S12. (a) Iron species in coarse aerosol particles in 2.1–4.2 μm fraction. Elemental maps of (b) Fe and (c) S obtained by microscopic XRF mapping. (d) Merged XRF map of Fe (red) and (blue). The spot with purple was the coexistence point of both elements. Green and white circles indicate measurement spots containing and not containing Fe(II)-sulfate and Fe(III)-sulfate, respectively.

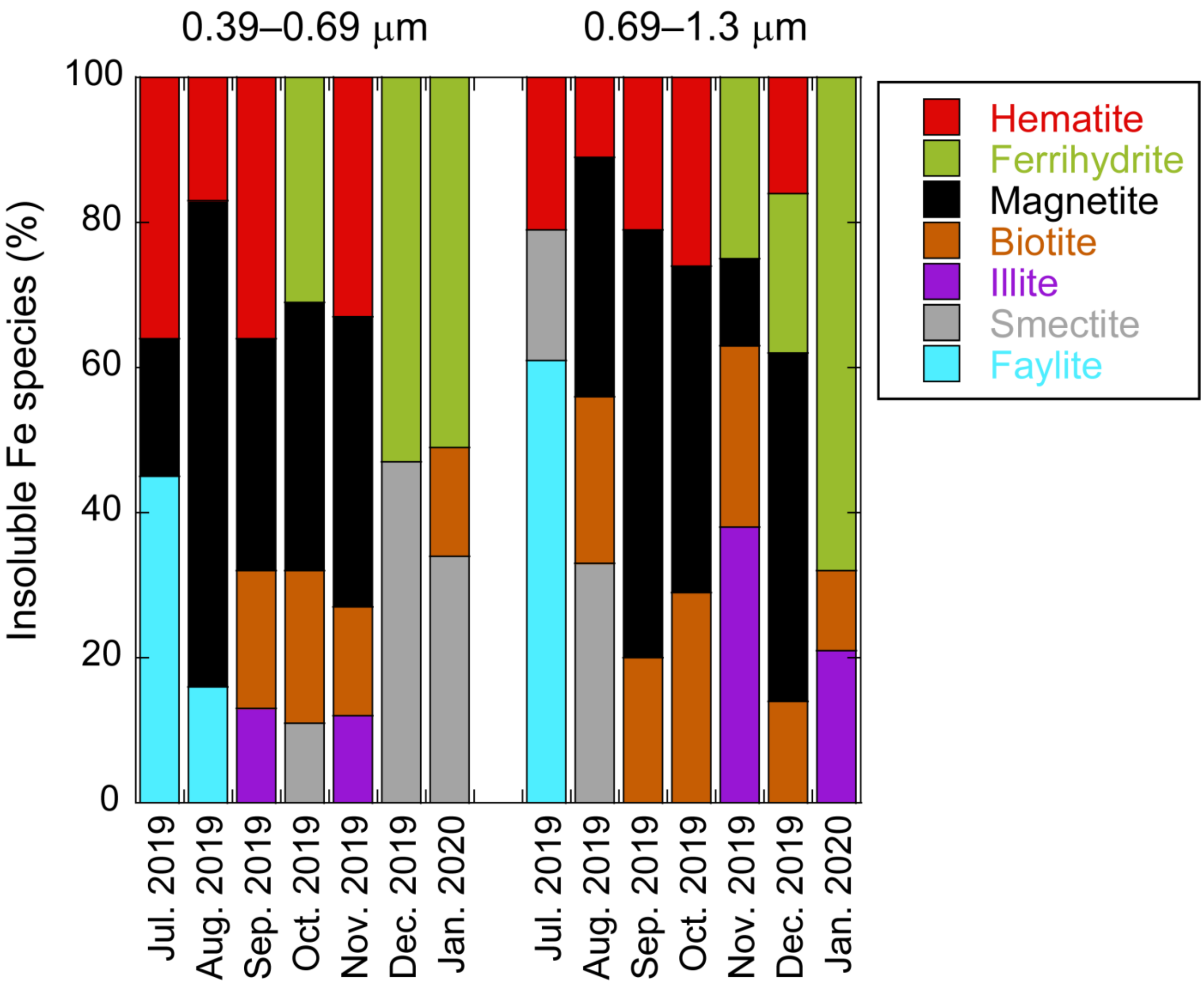

Figure S13. The insoluble Fe species in residues of water-extraction for fine aerosol particles (0.39–0.69 and 0.69–1.3 μm). Several Fe species, including faylite, were not detected by total Fe species determined by macroscopic XANES spectroscopy because the abundance of the Fe species is not sufficient to be detected by macroscopic XANES spectroscopy of T-Fe species.

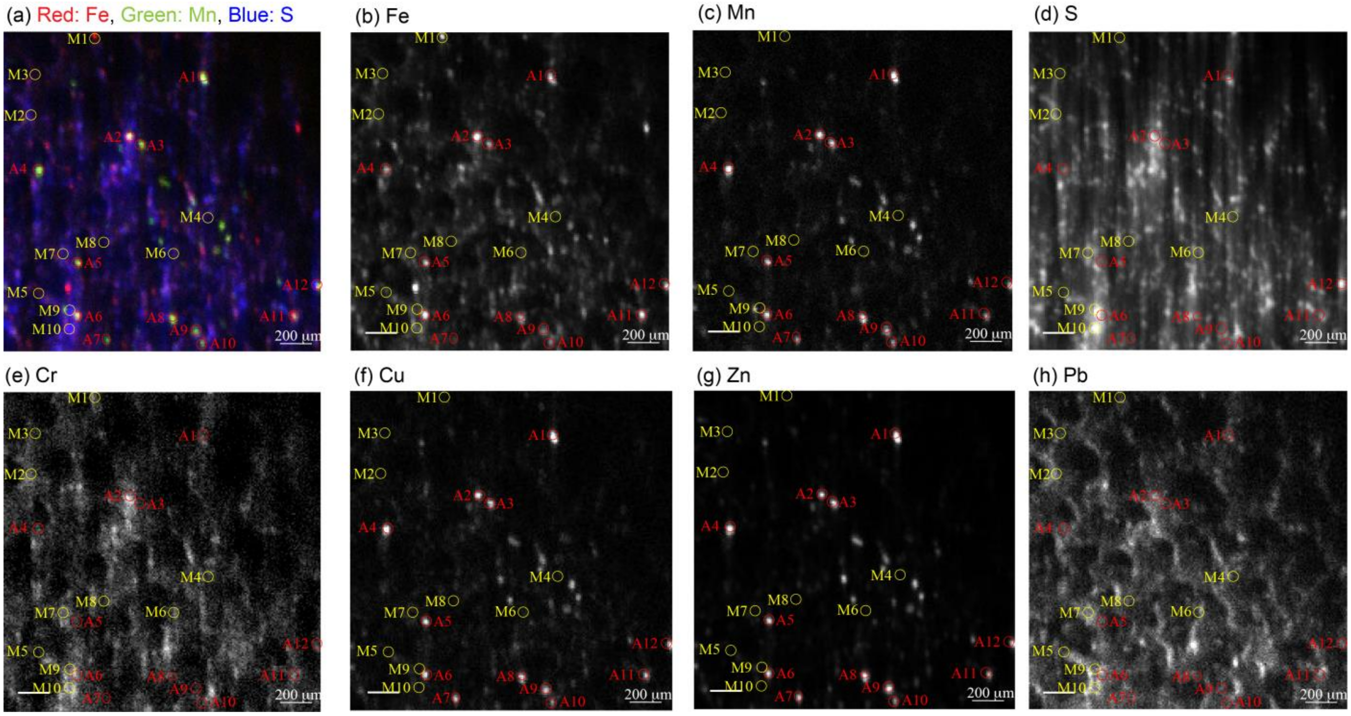
(a) Red: Fe, Green: Mn, Blue: S
(b) Fe
(c) Mn
(d) S
(e) Cr
(f) Cu
(g) Zn
(h) Pb

Figure S14. (a) Colored maps of Fe (red), Mn (green), and S (blue) in 0.39–0.69 µm aerosol particles collected in September 2019. Fine aerosol particles collected in September 2019. The normalized map of (b) Fe, (c) Mn, (d) S, (e) Cr, (f) Cu, (g) Zn, and (h) Pb. The red and yellow circles in these figures show measurement spots of mineral dust and anthropogenic aerosol.

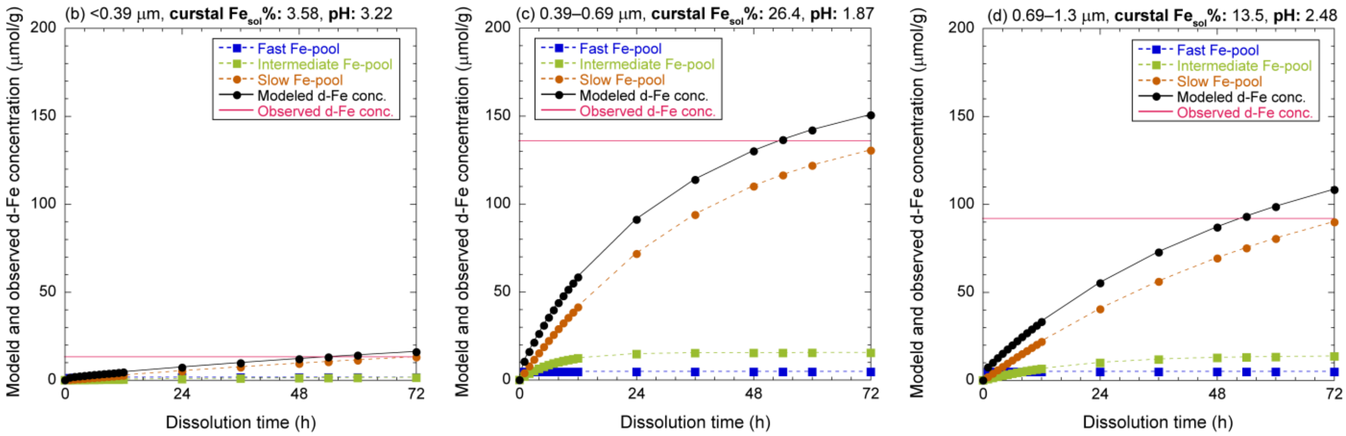

Figure S15. (a) Model parameter for the three Fe-pools model for the mineral dust of proton-promoted dissolutions. The example of the dissolution curve in each Fe pool (dashed line) and modeled d-Fe concentrations (black solid line) in (a) <0.39 μm, (b) 0.39–0.69 μm, and (c) 0.69–1.3 μm collected in January 2020. The dissolution curves were obtained assuming that the proton-promoted dissolution of Fe in mineral dust proceeds at a single $\mathrm{pH_{PPD}}$ with a reaction time of 54 hours.

Supplemental Table

Table S1. Sampling information for each sampling period.

Start time	End time	Total flow (m^3)	The state of COVID-19 lockdown
14:38, 10 July 2019	23:00, 17 July 2019	5899.0	
11:43, 14 August 2019	17:16, 28 August 2019	11526.1	
11:52, 6 September 2019	20:48, 13 September 2019	6111.5	
17:47, 18 October 2019	13:41, 25 October 2019	5513.5	
22:02, 15 November 2019	19:15, 22 November 2019	5704.0	
15:24, 18 December 2019	15:36, 27 December 2019	7296.9	
12:47, 24 January 2020	16:54, 31 January 2020	5870.5	During COVID-19 lockdown in China.
17:16, 19 February 2020	22:45, 26 February 2020	5934.7	Immediately after relaxation of the lockdown in China.
12:05, 18 March 2020	14:30, 25 March 2020	5823.9	
13:38, 24 April 2020	12:59, 1 May 2020	5718.4	Under the state of emergency declaration for COVID-19 in Japan. (e.g., Recommend restrictions on movement across the province）
11:13, 20 May 2020	10:47, 27 May 2020	5719.4	
13:32, 19 June 2020	14:27, 26 June 2020	5749.5	After the deregulating the state of emergency declaration in Japan.

Table S2 Certified and measurement values of NIES CRM No. 28 (Mori et al., 2008).

	Unit	Certified value	Measurement values
Na	%	0.796	0.785
Al	%	5.04	4.69
Ti	%	0.292	0.282
Ca	%	6.69	5.42
Fe	%	2.92	2.71
Zn	%	0.114	0.115
Mn	mg/kg	686	634
Cr	mg/kg	65.6	63.7
Cd	mg/kg	5.60	5.97
Pb	mg/kg	403	377

Table S3. The $\mathrm{Fe_{sol}}$% in TSP and $\mathrm{PM_{2.5}}$ collected in NOTOGRO and the Pacific Ocean.

Location	Extraction method*1	Sample	Sampling year	$\mathrm{Fe_{sol}}$%	Reference
NOTOGRO	Ultrapure water (B)	TSP	Nov. 2019–Apr. 2020 (EAout-period)	2.8–13.6% (average: 4.9%)	This study
NOTOGRO	Ultrapure water (B)	TSP	Jul.–Oct. 2019, May–Jun. 2020 (JPN-period)	6.4–17.4% (average: 11.6%)	This study
N. Pacific	Ultrapure water (I)	TSP	May–Jun. 2002	0.4–19.8% (average: 8.4%)	Buck et al. (2006)
N. Pacific	Ultrapure water (I)	TSP	Jun.–Aug. 2004	3.1–21.9% (average: 9.3%)	Buck et al. (2013)
N. Pacific	Seawater (SC)	TSP	April 2005 April 2006	2.4–5.6% (average: N.D.) 3.0–9.5% (average: N.D.)	Wu et al. (2007)
NW. Pacific	Ultrapure water	TSP	Feb. 2015	2.6–7.7% (average: 6.0%)	Sakata et al. (2022)
W. Pacific		TSP	Nov. 2010–Mar. 2011	4.5–10.6 (average: N.D.)	Xu et al. (2015)
Tropical Pacific	Seawater (SC)	TSP	April 2005	2.4%	Wu et al. (2007)
Pacific Ocean	Ultrapure water (I)	TSP	Jan.–Feb. 2005 (Southern hemisphere) Feb.–Mar. 2006 (Northern hemisphere)	3.8–29.1% (average: 9.7%)	Buck et al. (2013)
East China Sea	Ultrapure water (B)	TSP	Mar. 2005, Mar.–Apr. 2006, Nov. 2006, Mar.–Apr. 2007	N.D. (average: 1.4%, high Asian dust conc.) N.D. (average: 7.7%, low Asian dust conc.)	Hsu et al. (2010)
Yellow Sea	Ammonium acetate (B)	TSP	Mar.–Apr 2007	1.0–20% (average: N.D.) 1.0–2.6% (average: 1.7%, high Asian dust conc.)	Shi et al. (2013)
Yellow Sea		TSP	Feb.–Aug. 2009	0.1–15.7% (average: 4.3%)	Zhang et al. (2013)
NOTOGRO	Ultrapure water (B)	$\mathrm{PM_{2.1}}$	Nov. 2019–Apr. 2020 (EAout-period)	8.0–29.2% (average: 14.3%)	This study
NOTOGRO	Ultrapure water (B)	$\mathrm{PM_{2.1}}$	Jul.–Oct. 2019, May–Jun. 2020 (JPN-period)	15.5–49.5% (average: 35.5%)	This study
NW. Pacific	Ultrapure water (B)	$\mathrm{PM_{2.1}}$	Feb. 2015	8.2–20.2% (average: 14.2%)	Sakata et al. (2022)
NOTOGRO	Ultrapure water (B)	Coarse	Nov. 2019–Apr. 2020 (EAout-period)	0.5%	This study
NW. Pacific	Ultrapure water (B)	Coarse	Feb. 2015	3.5%	Sakata et al. (2022)

B: Batch dissolution, I: Instantaneous flow-through dissolution, SC: Semi-continuous flow-through dissolution

Table S4. Elemental concentration, in each factor for the JPN period estimated for PMF (ng/m^3). The EF$_{\text{T-Fe}}$, Fe$_{\text{sol}}$%, [d-Fe]/[d-Al], and [nss-SO$_4^{2-}$]/[T-Fe] were calculated using PMF-estimated concentrations. The r^2 shows the coefficient of determination between observation and modeled concentrations.

	Fresh dust	Aged dust	Steel industry	Heavy oil	Non-ferrous industry	Secondary aerosol	r^2
Na	15.147	3.932	0.000	1.705	1.851	1.428	0.98
Mg	2.01	0.625	0.227	0	0	0.290	0.96
Al	0.702	0.626	0.573	0.208	0	0	0.88
d-Al	0.078	0.221	0.031	0.031	0.078	0.066	0.95
K	2.27	0	1.41	2.30	1.15	1.09	0.84
Ca	0.798	0.481	0.148	0.320	0.116	0	0.98
Ti	0.049	0.123	0.015	0.018	0.038	0.007	0.94
V	0.004	0	0.047	0.125	0.020	0.016	0.96
Cr	0.005	0.006	0.020	0.009	0.014	0.001	0.96
Mn	0.038	0.040	0.119	0.020	0.000	0.052	0.97
Fe	0.590	0.693	1.155	0.202	0.080	0.497	0.96
Anthro-Fe	0.187	0.397	0.754	0.063	0.092	0.556	0.98
d-Fe	0.101	0.420	0.367	0	0.025	0.816	0.96
Co	3.16.E-04	2.59.E-04	7.85.E-04	5.60.E-04	4.74.E-04	0	0.98
Ni	0	0.008	0.029	0.050	0.020	0	0.97
Cu	0.010	0.019	0.058	0.025	0.009	0.002	0.74
Zn	0.239	0.194	0.437	0.333	0.045	0.229	0.86
Sr	0.012	0.011	0.007	0	0.005	0.006	0.92
Cd	0.00156	0.00295	0.00817	0.00227	6.41.E-04	7.50.E-05	0.93
Ba	0.016	0.005	0.029	0.015	0	0.018	0.83
Pb	0.067	0.035	0.151	0.037	0.005	0.072	0.94
SO$_4^{2-}$	0	48	0	105	41	281	0.98
EF$_{\text{T-Fe}}$	1.62	2.14	3.89	1.87	N.C. (*1)	N.C. (*1)	-
Fe$_{\text{sol}}$%	17.1	60.6	31.8	0.0	31.2	164.3	-
[d-Fe]/[d-Al]	0.62	0.92	5.67	0.00	0.15	5.98	-
[nssSO$_4^{2-}$]/[T-Fe]	0	22	0	274	220	320	-

*1. Not calculated (N.C.) EF$_{\text{T-Fe}}$ because PMF-estimated Al concentration was 0.

Table S5. Elemental concentration, in each factor for the EAout period estimated for PMF (ng/m^3). The EF$_{T\text{-}Fe}$, Fe$_{sol}$%, [d-Fe]/[d-Al], and [nss-SO$_4^{2-}$]/[T-Fe] were calculated using PMF-estimated concentrations. The r^2 shows the coefficient of determination between observation and modeled concentrations.

	Fresh dust	Aged dust	Steel industry	Heavy oil	Secondary aerosol	r^2
Na	23.965	0	0	3.158	3.635	0.93
Mg	3.517	0.693	0.030	0.202	0.646	0.99
Al	2.003	2.738	1.079	0.731	0.293	0.95
d-Al	0.170	0.247	0.244	0.026	0.202	0.91
K	1.409	2.292	3.325	3.217	2.645	0.77
Ca	1.352	1.010	0.625	0.429	0.058	0.99
Ti	0.099	0.229	0.169	0.014	0.000	0.98
V	0.003	0.004	0.015	0.017	0.003	0.60
Cr	0.007	0.008	0.022	0.025	0.001	0.46
Mn	0.054	0.064	0.162	0.035	0.024	0.96
Fe	0.896	1.839	2.716	0.315	0.111	0.98
Anthro-Fe	0.215	0.164	1.890	0.000	0.000	0.98
d-Fe	0.000	0.355	0.609	0.028	0.572	0.91
Co	0.000	0.002	0.000	0.000	0.001	0.88
Ni	0.000	0.004	0.024	0.025	0.000	0.87
Cu	0.008	0.007	0.039	0.048	0.015	0.86
Zn	0.204	0.093	0.569	0.369	0.161	0.83
Sr	0.028	0.035	0.024	0.000	0.003	0.94
Cd	0.001	0.002	0.006	0.003	0.003	0.81
Ba	0.044	0.016	0.014	0.023	0.004	0.90
Pb	0.058	0.025	0.257	0.139	0.111	0.87
SO$_4^{2-}$	18.960	25.717	69.630	62.380	159.120	0.94
EF$_{T\text{-}Fe}$	0.86	1.30	4.86	0.83	0.73	-
Fe$_{sol}$%	0	19.3	22.4	8.8	516.2	-
[d-Fe]/[d-Al]	0	0.694	0.200	0.506	1.369	-
[nssSO$_4^{2-}$]/[T-Fe]	0	8	15	82	726	-

References

Adachi, K., and Tainosho, Y.: Characterization of heavy metal particles embedded in tire dust, *Environ. Int.*, 30, 1009–1017, https://doi.org/10.1016/j.envint.2004.04.004, 2004.

An, J., Duan, Q., Wang, H., Miao, Q., Shao, P., Wang, J., and Zou, J.: Fine particulate pollution in the Nanjing northern suburb during summer: composition and sources, *Environ. Monit. Assess*, 187, 561, https://doi.org/10.1007/s10661-015-4765-2, 2015.

Apeagyei, E., Bank, M. S., and Spengler, J. D.: Distribution of heavy metals in road dust along an urban-rural gradient in Massachusetts, Atmos. Environ., 45, 2310–2323, https://doi.org/10.1016/j.atmosenv.2010.11.015, 2011.

Bibi, I., Singh, B., and Silvester, E.: Dissolution of illite in salineacidic solutions at 25°C, Geochim. Cosmochim. Ac., 75, 3237–3249, https://doi.org/10.1016/j.gca.2011.03.022, 2011.

Birmili, W., Allen, A. G., Bary, F., and Harrison, R. M.: Trace metal concentrations and water solubility in size-fractionated atmospheric particles and influence of road traffic, Environ. Sci. Technol., 40, 1144–1153, https://doi.org/10.1021/es0486925, 2006.

Bray, A. W., Oelkers, E. H., Bonneville, S., Wolff-Boenisch, D., Potts, N. J., Fones, G., and Benning, L. G.: The effect of pH, grain size, and organic ligands on biotite weathering rates, Geochim. Cosmochim. Ac., 164, 127–145, https://doi.org/10.1016/j.gca.2015.04.048, 2015.

Buck, C. S., Landing, W. M., and Resing, J.: Pacific Ocean aerosols: Deposition and solubility of iron, aluminum, and other trace elements, Mar. Chem., 157, 117–130, https://doi.org/10.1016/j.marchem.2013.09.005, 2013.

Buck, C. S., Landing, W. M., Resing, J. A., and Lebon, G. T.: Aerosol iron and aluminum solubility in the northwest Pacific Ocean: Results from 2002 IOC cruise, Geochem. Geophys. Geosyst., 7, Q04M07, https://doi.org/10.1029/2005GC000977, 2006.

Chen, C., Huang, L., Shi, J., Zhou, Y., Wang, J., Yao, X., Gao, H., Liu, Y., Xing, J., and Liu, X.: Atmospheric outflow of anthropogenic iron and its deposition to China adjacent seas, *Sci. Total Environ.*, 750, 141302, https://doi.org/10.1016/j.scitotenv.2020.141302, 2021.

Duvall, R. M., Majestic, B. J., Shafer, M. M., Chuang, P. Y., Simoneit, B. R. T. and Schauer, J. J.: The water-soluble fraction of carbon, sulfur, and crustal elements in Asian aerosols and Asian soils, Atmos. Environ., 42, 5872–5884, https://doi.org/10.1016/j.atmosenv.2008.03.028, 2008.

Fu, Z., Wu, Y., Zhao, S., Bai, X., Liu, S., Zhao, H., Hao, Y., Tian, H.; Emissions of multiple metals from vehicular brake linings wear in China, 1980–2020, 889, 164380, https://doi.org/10.1016/j.scitotenv.2023.164380, 2023.

Halle, L. L., Palmqvist, A., Kampmann, K., Jensen, A., Hansen, T., and Khan, F. R.: Tire wear particle and leachate exposures from a pristine and road-worn tire to Hyalella azteca: Comparison of chemical content and biological effects, Aquat. Toxicol., 232, 105769, https://doi.org/10.1016/j.aquatox.2021.105769, 2021.

Hsu, S. C., Liu, S. C., Arimoto, R., Shiah, F. K., Gong, G. C., Huang, Y. T., Kao, S. J., Chen, J. P., Lin, F. J., Lin, C. Y., Huang, J. C., Tsai, F., and Lung, S. C. C.: Effects of acidic processing, transport history, and dust and sea salt loadings on the dissolution of iron from Asian dust, *J. Geophys Res.*, 115, D19313, https://doi.org/10.1029/2009JD013442, 2010.

Itahashi, S., Hattori, S., Ito, A., Sadanaga, Y., Yoshida, N., and Matsuki A.: Role of dust and iron solubility in sulfate formation during the long-range transport in East Asia evidenced by ^{17}O-excess signatures *Environ. Sci. Technol.* 56, 13634–13643, https://doi.org/10.1021/acs.est.2c03574, 2022.

Ito, A., Ye, Y., Baldo, C., and Shi, Z.: Ocean fertilization by pyrogenic aerosol iron, npj Clim. Atmos. Sci., 4, 30, https://doi.org/10.1038/s41612-021-00185-8, 2021.

Jia, J., Chen, S., Yao, S., Xu, T., Zhang, T., Ma, Y., Wang, H., and Duan, W.: Emission characteristics and chemical components of size-segregated particulate matter in iron and steel industry, *Atmos. Environ.* 182, 115–127, https://doi.org/10.1016/j.atmosenv.2018.03.051, 2018.

Kajino, M., Hagino, H., Fujitani, Y., Morikawa, T., Fukui, T., Onishi, K., Okuda, T., Kajikawa, T., and Igarashi, Y.: Modeling transition metals in East Asia and Japan and its emission sources, GeoHealth, 4, e2020GH00259, https://doi.org/10.1029/2020GH000259, 2020.

Kodama, H. and Schnitzer, M.: Dissolution of chlorite minerals by fulvic acid, Can. J. Soil Sci., 53, 240–243, https://doi.org/10.4141/cjss73-036, 1973.

Kurokawa, J., and Ohara, T.: Long-term historical trends in air pollutant emissions in Asia: Regional emission inventory in Asia (REAS) version 3, Atmos. Chem. Phys., 20, 12761–12793, https://doi.org/10.5194/acp-20-12761-2020, 2020.

Li, J., Zhang, Y. L., Cao, F., Zhang, W., Fan, M., Lee, X., and Michaiski, G.: Stable sulfur isotopes revealed a major role of transition-metal ion-catalyzed SO_2 oxidation in haze episodes, *Environ. Sci. Technol.* 54, 2626–2634, https://doi.org/10.1021/acs.est.9b07150, 2020.

Li, R., Zhao, Y., Fu, H., Chen, J., Peng, M., and Wang, C.: Substantial changes in gaseous pollutants and chemical compositions in fine particles in the North China Plain during the COVID-19 lockdown period: anthropogenic vs. meteorological influences, Atmos. Chem. Phys., 21, 8677–8692, https://doi.org/10.5194/acp-21-8677-2021, 2022.

Li, R., Zhao, Y., Fu, H., Chen, J., Peng, M., and Wang, C.: Substantial changes in gaseous pollutants and chemical compositions in fine particles in the North China Plain during the COVID-19 lockdown period: anthropogenic vs. meteorological influences, *Atmos. Chem. Phys.*, 21, 8677–8692, https://doi.org/10.5194/acp-21-8677-2021, 2021.

Li, S., Zhang, B., Wu, D., Li, Z., Chu, S. Q., Ding, X., Tang, X., Chen, J., and Li, Q.: Magnetic particles unintentionally emitted from anthropogenic sources: Iron and steel plants, Environ. Sci. Technol., Lett., 8, 295–300, https://doi.org/10.1021/acs.estlett.1c00164, 2021.

Liu, T., Chan, A. W. H., and Abbatt, J. P. D.: Multiphase oxidation of sulfur dioxide in aerosol particles: Implications for sulfate formation in polluted environments, *Environ. Sci. Technol.*, 55, 4227–4242, https://doi.org/10.1021/acs.est.0c06496, 2021.

Liu, Y., Xing, J., Wang, S., Fu, X., and Zheng, H.: Source-specific speciation profiles of $PM_{2.5}$ for heavy metals and their anthropogenic emissions in China, *Environ. Pollut.*, 239, 544–544, https://doi.org/10.1016/j.envpol.2018.04.047, 2018.

Lowson, R. T., Comarmond, J., Rajaratnam, G., and Brown, P. L.: The kinetics of the dissolution of chlorite as a function of pH and at 25°C, Geochim. Cosmochim. Ac., 69, 1687–1699, https://doi.org/10.1016/j.gca.2004.09.028, 2005.

Mori, I., Sun, Z., Ukachi, M., Nagano, K., McLeod, C. Q., Cox, A. G., and Nishikawa, M.: Development and certification of the new NIES CRM 28: urban aerosols for the determination of multielements, Anal. Bioanal. Chem., 391, 1997–2003, https://doi.org/10.1007/s00216-008-2076-y, 2008.

Nriagu, J. O., and Pacyna, J. M.: Quantitative assessment of worldwide contamination of air, water and soils by trace metals, Nature, 134–139, https://doi.org/10.1038/333134a0, 1988.

Oakes, M., Ingall, E. D., Lai, B., Shafer, M. M., Hays, M. D., Liu, Z. G., Russell, A. G., and Weber, R. J.: Iron solubility related to particle sulfur content in source emission and ambient fine particles, Environ. Sci. Technol., 46, 6637–6644, https://doi.org/10.1021/es300701c, 2012.

Sakata, K., Kurisu, M., Takeichi, Y., Sakaguchi, A., Tanimoto, H., Tamenori, Y., Matsuki, A., and Takahashi, Y.: Iron (Fe) speciation in size-fractionated aerosol particles in the Pacific Ocean: The role of organic complexation of Fe with humic-like substances in controlling Fe solubility, Atmos. Chem. Phys., 22, 9461–9482, https://doi.org/10.5194/acp-22-9461-2022, 2022.

Sakata, K., Sakaguhci, A., Tanimizu, M., Takaku, Y., Yokoyama, Y., and Takahashi Y.: Idenitification of sources of lead in the atmosphere by chemical speciation using X-ray absorption near-edge structure (XANES) spectroscopy. *J. Environ. Sci.*, 26, 343–352, https://doi.org/10.1016/S1001-0742(13)60430-1, 2014.

Schroth, A. W., Crusius, J., Sholkovitz, E. R., and Bostick, B. C.: Iron solubility driven by speciation in dust sources to the ocean, Nat. Geosci., 2, 337–340, https://doi.org/10.1038/ngeo501, 2009.

Shi, J. H., Zhang, J., Gao, H. W., Tan, S. C., Yao, X. H., and Ren, J. L.: Concentration, solubility and deposition flux of atmospheric particulate nutrients over the Yellow Sea, *Deep Sea Res. II*, 97, 43–50, https://doi.org/10.1016/j.dsr2.2013.05.004, 2013.

Shupert, L. A., Ebbs, S. D., Lawrence, J., Gibson, D. J., and Filip, P.: Dissolution of copper and iron from automotive brake pad wear debris enhances growth and accumulation by the invasive macrophyte Salvinia molesta Mitchell, Chemosphere, 92, 45–51, https://doi.org/10.1016/j.chemosphere.2013.03.002, 2013.

Wang, S. X., Zhao, B., Cai, S. Y., Klimont, Z., Nielsen, C. P., Morikawa, T., Woo, J. H., Kim, Y., Fu, X., Xu, J. Y., Hao, J. M., and He, K. B.: Emission trends and mitigation options for air pollutants in East Asia, Atmos. Chem. Phys., 14, 6571–6603, https://doi.org/10.5194/acp-14-6571-2014, 2014.

Wu, J., Rember, R., and Cahill, C.: Dissolution of aerosol iron in the surface waters of the North Pacific and North Atlantic oceans as determined by a semicontinuous flow-through reactor method, *Global Biogeochem. Cy.*, 21, GB4010, https://doi.org/10.1029/2006GB002851, 2007.

Xu, G., and Gao, Y.: Characterization of marine aerosols and precipitation through shipboard observations on the transect between 31°N–32°S in the West Pacific, *Atmos. Pollut. Res.*, 6, 151–161, https://doi.org/10.5094/APR.2015.018, 2015.

Zhang, T. R., Shi, J. H., Gao, H. W., Zhang, J., and Yao, X. H.: Impact of source and atmospheric processing on Fe solubility in aerosols over the Yellow Sea, China, *Atmos. Environ.*, 75, 249–256, https://doi.org/10.1016/j.atmosenv.2013.04.021, 2013.

Zheng, H., Kong, S., Chen, N., Yan, Y., Liu, D., Zhu, B., Xu, K., Cao, W., Ding, Q., Lan, B., Zhang, Z. Zheng, M., Fan, Z., Cheng, Y., Zheng, S., Yao, L., Bai, Y., Zhao, T., and Qi, S.: Significant changes in the chemical compositions and sources of PM2.5 in Wuhan since the city lockdown as COVID-19, Sci. Total Environ., 739, https://doi.org/10.1016/j.scitotenv.2020.140000, 140000, 2020.